Journal of Applied Physics TUTORIAL scitation.org/journal/jap

Tutorial: Real-time coherent terahertz imaging of objects moving in one direction with constant speed

Cite as: J. Appl. Phys. **133**, 211102 (2023); doi: 10.1063/5.0147777
Submitted: 25 February 2023 · Accepted: 15 May 2023 ·
Published Online: 1 June 2023

Takeshi Yasui[1,a)] and Emmanuel Abraham[2]

AFFILIATIONS

[1]Institute of Post-LED Photonics (pLED), Tokushima University, 2-1 Minami-Josanjima, Tokushima 770-8506, Japan
[2]Laboratoire Ondes et Matière d'Aquitaine (LOMA), University of Bordeaux, Talence Cedex 33405, France

[a)]**Author to whom correspondence should be addressed:** yasui.takeshi@tokushima-u.ac.jp

ABSTRACT

Pulsed terahertz (THz) electric fields enable various coherent THz imaging modes, such as reflection tomography, spectral imaging, and computed tomography (CT) for nondestructive inspection, quality control, and material characterization. The extension of coherent THz imaging modes to moving objects has been regarded as key to their social implementation. This Tutorial focuses on two-dimensional spatio-temporal (2D-ST) THz imaging of objects moving in one direction with constant speed as a promising means of enabling real-time coherent THz imaging. In 2D-ST THz imaging, the temporal waveform and line image of the THz pulse are simultaneously acquired without the need for mechanical scanning of the time delay and sample position using a combination of non-collinear 2D free-space electro-optic sampling with THz line-imaging optics. This 2D-ST THz imaging boosts the imaging rates of THz reflection tomography, THz spectral imaging, and THz CT to levels that are applicable to moving objects. The advanced THz reflection tomography and THz spectral imaging that result from the assistance of 2D-ST THz imaging achieve real-time line imaging of cross sections and spectral signatures, respectively. Subsequently, this enables in-line total inspection of objects moving on a translation stage or a conveyor belt. A THz CT system using real-time line projection of a THz beam is effectively applied to a 2D spectral cross section of a continuously rotating object. 2D-ST THz imaging enables the functional THz imaging of moving objects in various practical applications.

I. INTRODUCTION

Terahertz (THz) imaging with a pulsed electric field, namely, coherent THz imaging, has attracted attention as a new tool for nondestructive inspection, quality control, and material characterization owing to its non-contact, non-ionizing, and coherent imaging.[1–4] Several types of imaging modes have been reported, such as shadowgraphs,[5] reflection tomography,[6] spectral imaging,[7] computed tomography (CT),[8] and microscopy.[9] However, the requirement for the real-time imaging often becomes a bottleneck when implementing these imaging modes in real-world applications. One obstacle to real-time imaging is the necessity of mechanical time-delay scanning for temporal waveform measurements of pulsed THz electric fields or THz pulses. The typical acquisition time of a temporal waveform is approximately a few minutes when a stepping-motor-driven translation stage is used for time-delay scanning. Another obstacle to real-time imaging is the use of a point detector, such as a photoconductive antenna. To obtain a two-dimensional (2D) image, the sample position must be raster-scanned in the focal spot of the THz beam by multiple translation stages whenever the acquisition of the THz temporal waveform is completed. The total acquisition time of 2D imaging increases from tens of minutes to several hours, depending on the number of image pixels, because the mechanical scanning operations of time delay and sample position must be performed sequentially. Consequently, coherent THz imaging has thus far only been applied to stationary objects. The potential applications for coherent THz imaging in industry would greatly increase if these techniques can be extended to moving objects.

One effective method to reduce the acquisition time of the temporal waveform is to use a fast scanner for the mechanical time delay, such as a galvanometric scanner, piezoelectric stage, or rotating delay line.[3] However, these mechanical methods have several drawbacks, such as mechanical vibrations, spot size variation in the laser light, and/or a trade-off issue between the scanning range and scanning rate. The asynchronous-optical-sampling (ASOPS) method[10,11] or electronically controlled optical sampling (ECOPS)[12,13] appears to be a promising method to accomplish rapid time-delay scanning because mechanical time-delay scanning is not required. However, the need for a pair of ultrashort pulse lasers with slightly different or exactly equal repetition rates has undermined the versatility of the ASOPS method or the ECOPS method. One effective method to eliminate the need for 2D mechanical scanning of sample positions is 2D free-space electro-optic sampling (2D-FSEOS).[14] In 2D-FSEOS, the THz-image-encoded near-infrared (NIR) light can be read as a 2D THz image of a sample in real-time using an NIR camera. This is because the 2D THz image is encoded to an NIR probe beam in an electro-optic (EO) crystal using the Pockels effect. Another effective method for full-field 2D THz imaging is THz compressed sensing with a single-pixel fiber-coupled photoconductive antenna, achieving a THz video with 32×32 resolution and six frames per second.[15] However, these two methods still require the mechanical time-delay scanning in coherent THz imaging modes, except for shadowgraphs; they are also incompatible with ASOPS and ECOPS because of the low repetition rate of the laser pulse for the 2D-FSEOS and the temporal multiplex of repetitive spatial encoding and rapid time-delay scanning for the THz compressive sensing.

Real-time line imaging is sufficient for application to objects moving by a translation stage or on a conveyor belt because a series of continuously acquired line images that depend on the sample movement correspond to a 2D image of the moving object. Rapid acquisition of THz line images can be achieved if an alternative technique is used to simultaneously measure the time delay and sample position, instead of using mechanical stages. One effective method for realizing a stage-free configuration is the combination of a single-shot measurement of the temporal waveform and its line imaging in a THz pulse, enabling real-time 2D spatiotemporal (2D-ST) THz imaging. The 2D-FSEOS approach can be extended to 2D-ST THz imaging by modifying the optical configuration. The non-collinear configuration of the THz and NIR probe beams replaces the collinear configuration in 2D-FSEOS and enables the time-to-space conversion of the THz pulse. Subsequently, the resulting line image is encoded onto the NIR probe beam as a temporal waveform of the THz pulse.[16] This type of non-collinear 2D-FSEOS was used for a single-shot measurement of the temporal waveform in a THz pulse, requiring no mechanical stage for the time delay. This was further extended into a 2D-ST THz imaging technique based on the combination of non-collinear 2D-FSEOS and line focusing of a THz beam onto a sample.[17] This 2D-ST THz imaging technique achieved, for the first time, functional THz imaging of objects moving in one direction with constant speed, such as THz reflection tomography,[17] THz spectral imaging,[18,19] and THz CT.[20,21]

This Tutorial focused on 2D-ST THz imaging and its application to three coherent THz imaging modes that are applicable to moving objects. The principle of operation for 2D-FSEOS, non-collinear 2D-FSEOS, and 2D-ST THz imaging is described in Sec. II. Real-time THz reflection tomography and its application to paint films are presented in Sec. III. A THz spectral imaging system using the real-time line scanning of a THz beam and its application to moving objects are described in Sec. IV. The effective application of fast THz CT with real-time line projection to spectral 2D cross-sectional imaging of continuously rotating objects and 3D volumetric imaging is described in Sec. V. Finally, the paper is summarized in Sec. VI.

II. PRINCIPLE OF OPERATION

A. 2D-FSEOS: Transfer of THz image onto NIR light

A schematic of the Pockels effect in an EO crystal is shown in Fig. 1. The Pockels effect is a phenomenon in which an isotropic dielectric crystal exhibits birefringence due to the anisotropic change in the refractive index in proportion to the strength of the electric field when an electric field is applied. Here, the case where a +45° linearly polarized light is incident on the EO crystal is considered. The +45° linearly polarized light is vector-decomposed into horizontal and vertical polarization components (+0° and +90°), denoted as red and blue, respectively, in Fig. 1. These two orthogonal polarization components are propagated in phase. They also experience the same refractive index in the crystal owing to isotropic crystallinity and maintain the in-phase condition when they are incident on the EO crystal without an external electric field. However, only the refractive index along the vertical axis changes linearly if an external electric field is applied to the vertical axis of the crystal (yellow arrow in Fig. 1), depending on the applied electric field via the Pockels effect. In this case, the two orthogonal polarization components propagate the EO crystal out of phase because they experience different refractive indices for the EO crystal, namely, birefringence. The output light from the EO crystal does not exhibit +45° linear polarization, instead exhibiting different polarizations depending on the external electric field. For example, the polarization was +135° when the external electric field induced a phase delay of the vertical polarization component by π in the EO crystal (namely, half-wavelength electric field). Benefiting from the ultrafast response, Pockels-effect-based EO crystals, such

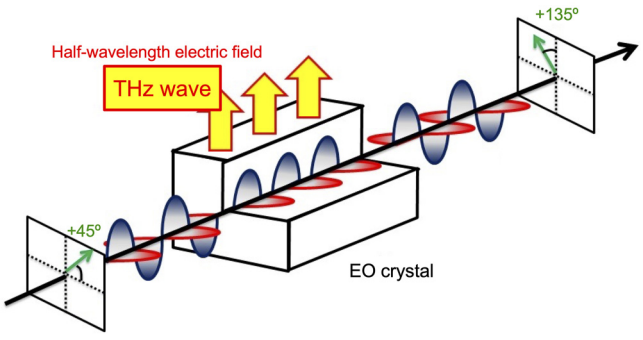

FIG. 1. Pockels effect in an EO crystal.

as lithium niobate ($LiNbO_3$), have been widely used as optical modulators of amplitude or phase in the field of optical communication.

The Pockels effect can also be used for the detection of THz electric fields, namely, free-space electro-optic sampling (FSEOS).[22] In this case, the free-space propagating THz pulse will function as an external electric field in a specific EO crystal. For example, zinc telluride (ZnTe) crystal has been widely used for FSEOS because it has a relatively high EO coefficient, moderate transmission of THz pulse, and a small phase mismatching between THz pulse and NIR probe pulse. The polarization measurement of the NIR probe light is equivalent to the electric field measurement of the THz pulse because the polarization of the NIR probe light propagating in the crystal changes depending on the THz electric field. The combination of polarization and pump–probe measurements enables a temporal waveform measurement of the THz electric field. A typical FSEOS configuration is shown in Fig. 2(a). The THz pulse and linearly polarized probe beams are spatially overlapped by a beam splitter, thus becoming collinearly or coaxially incident on the EO crystal. The polarization of the probe light changed depending on the THz electric field, as shown in Fig. 2(b), when the polarization angles of the THz pulse and probe light were suitably adjusted to the crystal axis of the EO crystal. As the temporal width of the probe light is shorter than that of the THz pulse, the pump–probe measurement of polarization in the probe light enables the temporal sampling of the instantaneous THz electric field with a resolution equal to the temporal width of the probe light. The linear polarization of the probe light was converted into circular polarization by a quarter-wave plate (λ/4) to magnify the change in birefringence induced by the THz electric field. Subsequently, a small distortion of the circular polarization induced by the THz electric field was sensitively detected by the combination of a Wollaston prism (P) and a balanced photodetector.

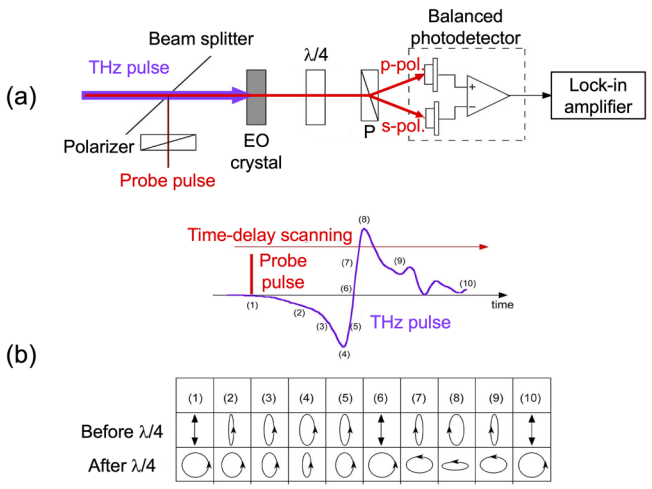

FIG. 2. Free-space electro-optics sampling (FSEOS). (a) Optical setup of FSEOS. (b) Temporal change of polarization in probe pulse induced by the pulsed THz electric field.

An important advantage of FSEOS over a photoconductive antenna is its extensibility for 2D imaging, namely, 2D-FSEOS. A schematic of the experimental setup for the 2D-FSEOS is shown in Fig. 3. A sample was irradiated with a large-diameter, high-power THz beam generated by the optical nonlinear effect of an amplified femtosecond NIR pump light in an optical nonlinear crystal (not shown). The THz beam passing through the sample formed a THz image of the sample on the EO crystal using a THz lens. This resulted in the 2D spatial distribution of the THz-induced birefringence in the EO crystal. A large-diameter, linear-polarized NIR probe beam experiences a 2D spatial distribution of THz-induced birefringence in the EO crystal when it is incident on the crystal in synchronization with the THz pulse. The linear-polarized probe beam after passing through a polarizer (P) is converted into the elliptical-polarized one in proportion to the THz electric field in the EO crystal, and its orthogonal component is extracted with an analyzer (A). In this way, the 2D spatial distribution of the THz-induced birefringence in the EO crystal is converted into that of the probe light intensity when a pair of P and A are positioned in a cross-Nicol arrangement to sandwich the EO crystal. In other words, the THz image of the sample was transferred into a large-diameter NIR probe beam as the 2D distribution of the optical intensity. The resulting probe-beam image was read using an NIR camera. Key parameters of the NIR camera are high speed, high intensity-resolution, and low dark noise to adopt a dynamic-subtraction mode[23] described later in order to improve a signal-to-noise ratio (SNR) of the image. In this way, a 2D THz image of the sample could be obtained in real-time without the need for sample-position scanning.

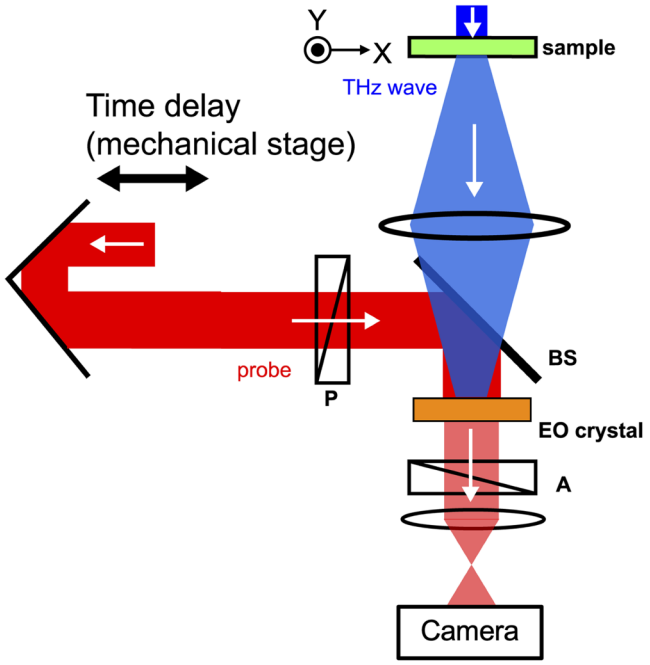

FIG. 3. Optical setup of 2D-FSEOS.

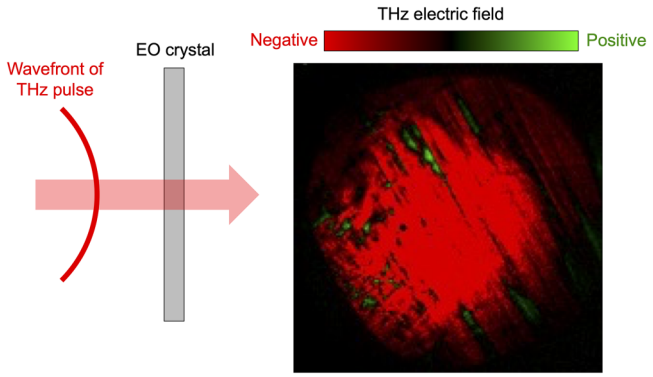

FIG. 4. Propagation of spherical wavefront in the focused THz beam measured by 2D-FSEOS. Multimedia available online.

2D-FSEOS was used to visualize a temporal evolution of an electric field in a focused THz pulse. A temporal variation in the THz electric field when the probe light was continuously time-delayed with respect to the THz pulse is shown in Fig. 4 (Multimedia view). The movie clearly shows the temporal evolution of the spherical wavefront in the focused THz beam. The temporal behavior of the THz electric field was similar to that of ripples on the water surface.

B. Non-collinear 2D-FSEOS: Time-to-space conversion of THz pulse

2D-FSEOS can be used for the time-to-space conversion of THz pulses when a large-diameter THz beam is crossed as a plane with a large-diameter NIR probe beam in the EO crystal,[16] namely, non-collinear 2D-FSEOS. A principle of operation for non-collinear 2D-FSEOS is shown in Fig. 5. The probe beam can be

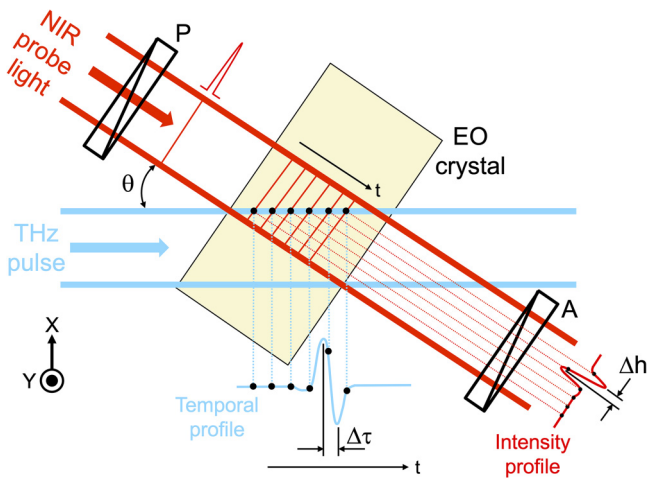

FIG. 5. Non-collinear 2D-FSEOS for the time-to-space conversion of the THz pulse.

considered to have a single wavefront (red line) when the pulse duration of the probe beam is sufficiently shorter than that of the THz beam. In contrast, the THz beam has a temporally spread wavefront (see blue lines) compared to the single wavefront of the probe pulse. The single wavefront of the probe beam and the temporally spread wavefront of the THz beam are incident on the EO crystal at a crossed angle of θ in air. The temporally spread wavefront of THz beam overlaps at different transverse positions of the beam cross section in the single wavefront of the probe beam at different times. We here define the propagation speeds of the THz and probe beams in the EO crystal as v_{THz} and v_{probe}, respectively. The THz beam propagates at a speed of $v_{THz}\bullet\cos\theta$, along the propagation direction of the probe beam through the EO crystal. If $v_{probe} = v_{THz}\cos\theta$, then the THz and probe beams propagate through the EO crystal while maintaining the same overlap condition. As a result, the time delay ($\Delta\tau$) of the THz beam is converted into the spatial distribution (Δh) of the polarization in the probe beam via 2D-FSEOS, which is expressed as

$$\Delta\tau = \frac{\Delta h \cdot \tan\theta}{c}, \tag{1}$$

where c is the speed of light. Although the diffraction of THz beam at the surface of the ZnTe crystal leads to some errors in the time-to-space conversion of Eq. (1), it is negligible in the following experiments. Finally, the temporal waveform of the THz pulse can be read as a line image of the probe beam intensity using crossed Nichol prisms and an NIR camera. We set the best crossing angle within the limits of THz-pulse beam diameter, NIR-probe beam diameter, and crystal size to obtain a large size of the line image. Although the phase mismatching between THz and probe beams depends on the incident angle of both beams to the crystal, the degradation of time resolution by the phase mismatching is negligible due to the thin crystals used. In order to avoid the non-uniformity of the residual birefringence inherent in the crystal, the irradiation positions of both beams on the crystal were adjusted. The configuration without the need for time-delay scanning enables the real-time measurement of the temporal waveform in the THz pulse at the camera frame rate and even the single-shot measurement at the pulse repetition rate.

Non-collinear 2D-FSEOS was used to obtain a temporal waveform of the THz pulse generated by the optical rectification of a femtosecond Ti:sapphire regenerative amplifier pulse (center wavelength = 800 nm, pulse duration = 100 fs, repetition rate = 1 kHz, pulse energy = 1 mJ) in a ZnTe crystal (size = 10 × 10 mm^2, thickness = 4 mm). 2D images of the probe beam with a THz beam (size = 640 × 480 p, frame rate = 10 Hz) are shown in Fig. 6(a), in which the horizontal coordinate indicates the time axis. The time window size was 9 ps from the probe beam diameter and crossed angle, based on Eq. (1). The pixel resolution corresponding to the sampling time interval was 14 fs from the time window size and number of camera pixels. The THz pulse appeared as a vertical white line. A 3D visualization of the probe beam image with a THz beam is shown in Fig. 6(b), in which the temporal waveform of the pulsed THz electric field developed along the vertical direction. The intensity profile along the red line of the image in Fig. 6(b) is shown in Fig. 6(c). A pulse duration of 0.5 ps was observed with an

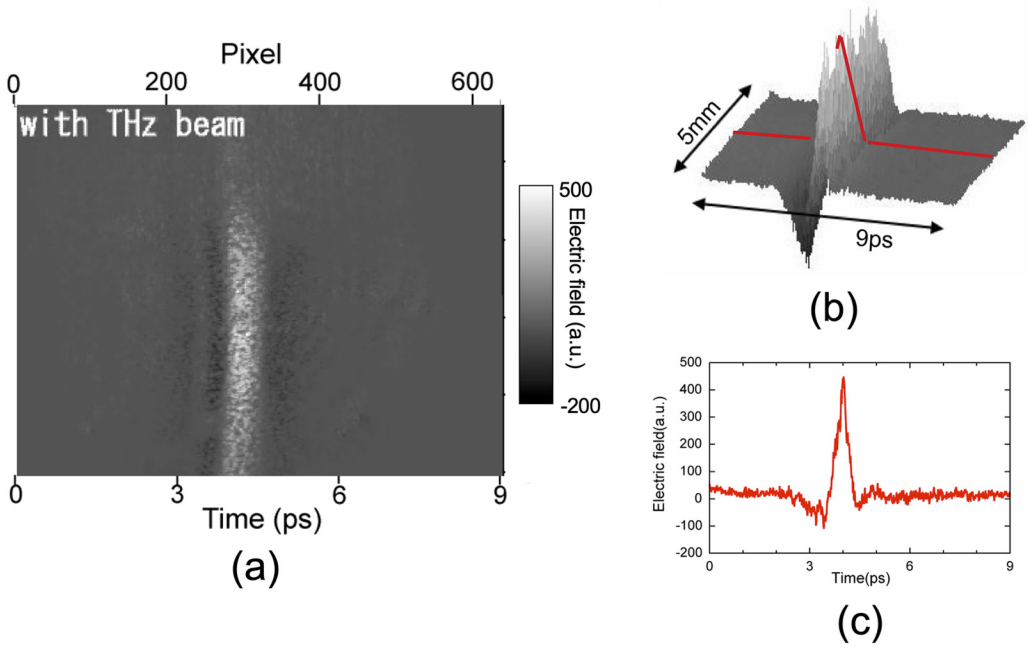

FIG. 6. Temporal waveform measurement of the THz pulse by non-collinear 2D-FSEOS. (a) 2D image of probe beam with THz beam and (b) its 3D representation. (c) Temporal waveform of THz pulse extracted from a red line of Fig. 6(b).

SNR of 80. In the 2D camera image of Fig. 6(a), it is important to note that only a horizontal coordinate is used for the temporal measurement of THz pulse, whereas a vertical coordinate is redundant. This redundancy enables the extension of non-collinear 2D-FSEOS to 2D-ST THz imaging.

C. 2D-ST THz imaging: Combination of THz pulse measurement and THz line imaging

One dimension along the horizontal coordinate is used to measure the spatial distribution of the THz-induced birefringence corresponding to the temporal waveform of the pulsed THz electric field. The remaining one dimension along the vertical coordinate is used for the THz line imaging of a sample with the assistance of THz line-imaging optics. To combine them, we constructed the optical setup of 2D-2T THz imaging as shown in Fig. 7. A large-diameter, intense THz pulse was focused onto the sample by the first THz cylindrical lens (CL1, f = 50 mm), resulting in a line of illumination along the y axis of the sample (length of the THz focal line = 20 mm). The THz beam was then incident on a 1-mm-thick, 25-mm-square, ⟨110⟩ ZnTe crystal (ZnTe) used for 2D-ST THz imaging after it had passed through a THz plano–convex lens (L, $f = 100$ mm) and a second THz cylindrical lens (CL2, $f = 100$ mm). As a result of these optics, the THz beam incident on ZnTe was collimated in the top view, whereas it was imaged in the side view (the imaging ray indicated by the green broken line). Meanwhile, a probe beam was expanded to approximately 30 mm in diameter using a beam expander (not shown) and then linearly polarized using a polarizer (P). The probe and THz beams were non-collinearly incident on ZnTe for 2D-ST THz imaging. The spatial distribution of the polarization state was converted into a spatial intensity distribution using two crossed polarizers (P and A). The resulting 2D image of the probe beam was acquired using a high-speed CMOS camera (232 × 232 p, maximum frame rate = 1000 frame/s). It is important to note that real-time THz line imaging (y axis) is sufficient for THz imaging of a moving object when the object is moving in one direction (x axis) at a constant speed on a translation stage. This is because a 2D THz image of the

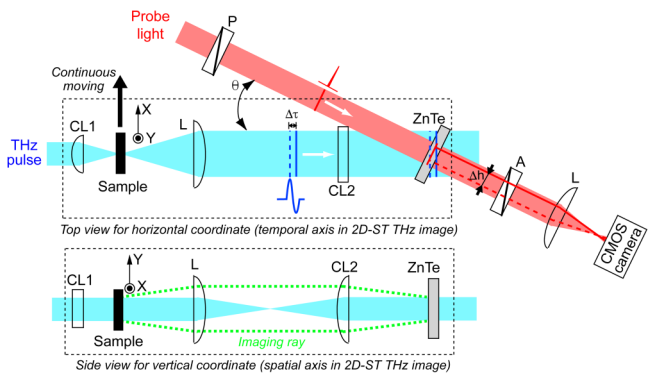

FIG. 7. Optical setup of 2D-ST THz imaging.

object can be created as a series of THz line images if the THz line image can be acquired in real-time, depending on the object movement. The combined use of THz pulse measurement and THz line imaging enables the 2D-ST THz imaging of a sample. 2D-ST THz imaging is equivalent to real-time THz line imaging with the temporal information of THz pulses. Therefore, its reflection configuration can be used for the THz reflection tomography of moving objects with line focusing.[17] Furthermore, its transmission configuration can be used for real-time THz line imaging with the spectral information of the THz pulse if the time axis of the 2D-ST THz image is Fourier-transformed by a computer while maintaining the spatial information of the THz line image, that is, real-time THz spectral line imaging. This can be used for real-time THz spectral imaging of moving objects[18,19] and rapid THz spectral CT.[20,21]

We acquired 2D-ST THz image using the experimental setup of Fig. 7. The 2D-ST THz line image could be acquired at a frame rate of 500 Hz. An example of a 2D-ST THz image (232 × 232 p) without a sample after integrating 50 images (corresponding measurement time = 100 ms) is shown in Fig. 8(a). Here, the horizontal and vertical dimensions indicate the time (window size = 34 ps, pixel resolution = 147 fs) and space (window size = 20 mm, pixel resolution = 86 μm) coordinates, respectively. The temporal waveform of the pulsed THz electric field extracted from the horizontal blue line of the 2D-ST THz image in Fig. 8(a) is shown in Fig. 8(b). A pulse duration of 0.38 ps was obtained at an SNR of 403. The time resolution of this 2D-ST THz image is theoretically determined by the pulse duration of the NIR probe beam assuming the negligible phase mismatching between THz pulse beam and NIR probe beam in the ZnTe crystal. Conversely, the spatial resolution of 2D-ST THz image depends on a numerical aperture of THz line imaging optics (see the imaging ray in Fig. 7). The detailed evaluation of spatial resolution is given elsewhere.[18] The limited size of the ZnTe crystal is also a bottleneck of both resolution improvement. The maximum acquisition rate of 2D-ST THz image is limited by a laser pulse rate (=1 kHz) because 2D-ST THz image can be acquired in a single-shot measurement. If the object is moving at a higher speed compared with the acquisition rate, the spatial resolution along the moving direction will be worse and the image blur will appear due to the temporal integration of successively moving THz lines.

The THz spectral line images of the amplitude and phase that were produced by Fourier-transforming the time axis of the 2D-ST THz image in Fig. 8(a) are shown in Figs. 9(a) and 9(b), respectively. Here, the horizontal and vertical dimensions indicate the frequency (window size = 3 THz, pixel resolution = 26 GHz) and space (window size = 20 mm, pixel resolution = 86 μm) coordinates, respectively. The THz spectra of the amplitude and phase extracted from the horizontal white line in the THz spectral line images of the amplitude and phase cover a spectral range of 3 THz and are shown in insets of Figs. 9(a) and 9(b), respectively.

III. REAL-TIME THZ REFLECTION TOMOGRAPHY OF PAINT FILM

It is important to visualize the internal structures of an object as a cross-sectional image in the field of non-destructive testing. Although x rays and ultrasonic waves have been utilized for this purpose in industrial and biomedical applications, the contact

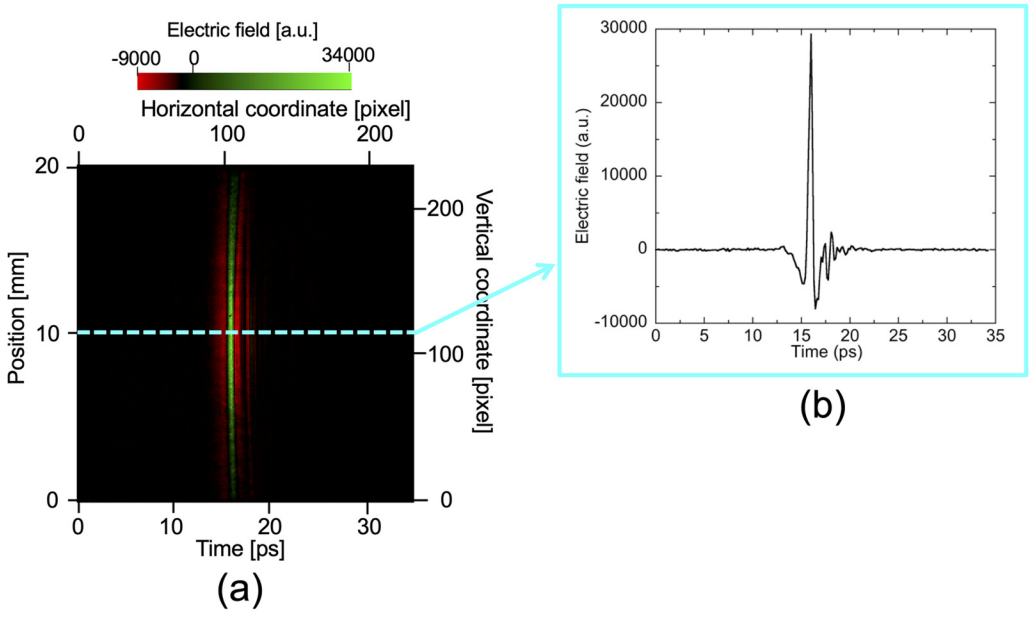

FIG. 8. (a) 2D-ST THz image without a sample (size = 232 pixels by 232 pixels, measurement time = 100 ms) and (b) temporal waveform of pulsed THz electric field extracted from a horizontal blue line of 2D-ST THz image in Fig. 8(a).

measurement and respective ionizing effect that is harmful to human health can limit certain applications. THz reflection tomography has attracted attention as a complementary tool for these conventional methods because it can serve as a non-ionizing and non-contact probe. THz reflection tomography is realized by the time-of-flight measurement of THz pulse echoes when a THz pulse is incident on a sample in a reflection geometry. This technique has been used to visualize the internal structure of floppy disks,[6] pharmaceutical tablet coatings,[24] automobile paint,[25,26] and skin cancer.[27] For example, THz reflection tomography has been successfully applied for the determination of painting thickness and its distribution in various kinds of paint films that can be hardly measured by conventional thickness meters.[25] Furthermore, the monitoring of dryness in a wet paint film has been demonstrated by taking advantage of a distinct spectroscopic difference in the THz region between the wet and dry conditions of a paint film. However, its application to moving objects is limited by the slow image acquisition rate. If the THz reflection tomography is achieved in real time, it opens the door to in-process or in-line monitoring of the paint film in industrial products. In this section,

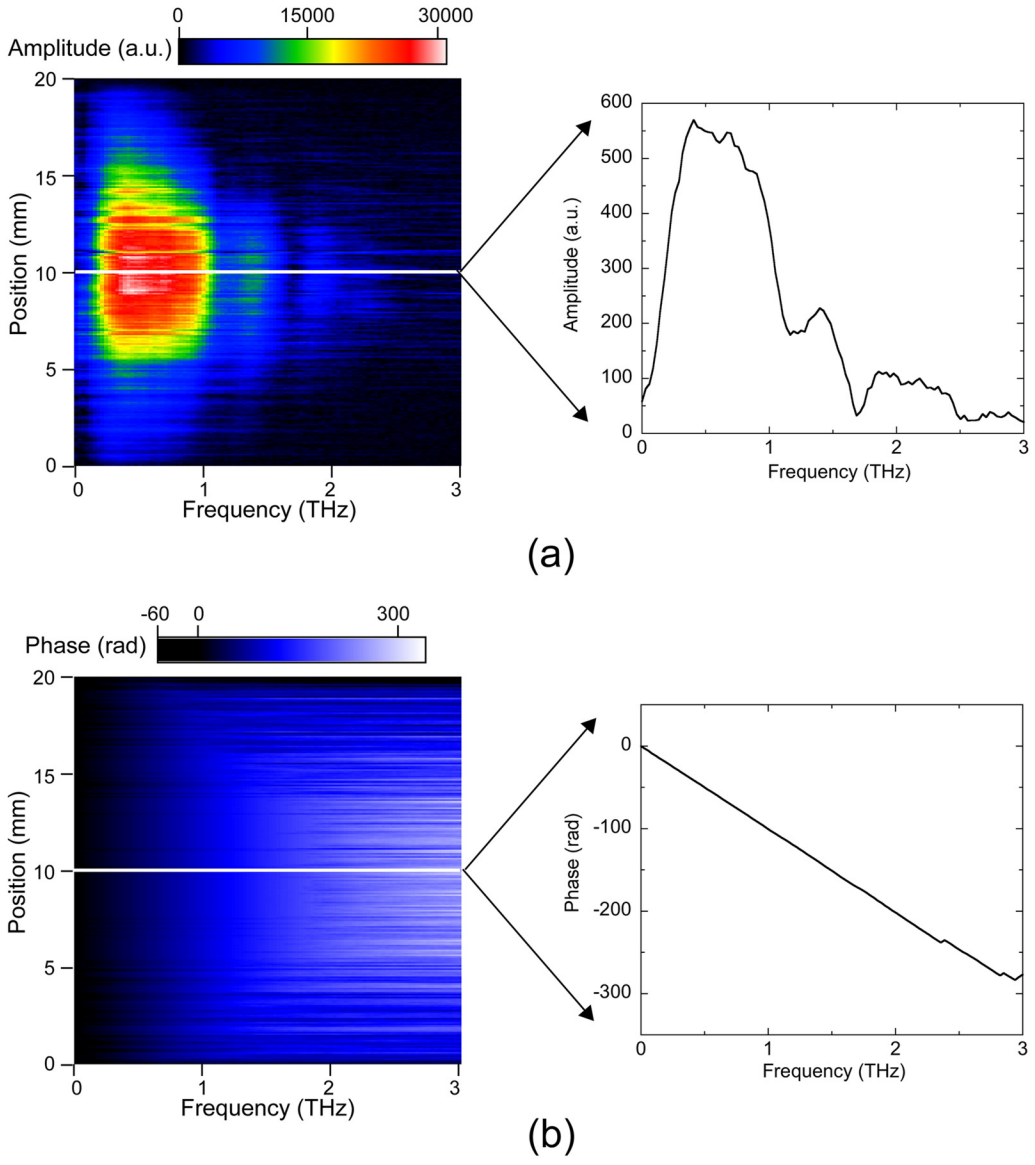

FIG. 9. (a) THz spectral line image of the amplitude and THz amplitude spectrum extracted along the white line. (b) THz spectral line image of the phase and THz phase spectrum extracted along the white line.

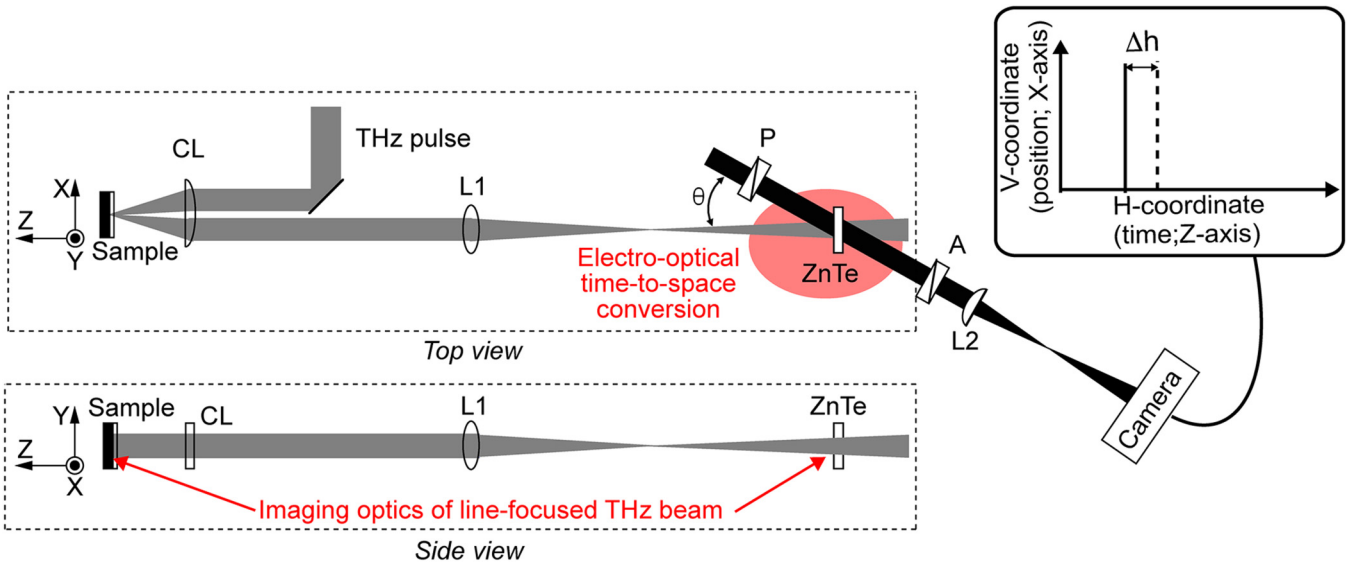

FIG. 10. Experimental setup of real-time THz reflection tomography based on 2D-ST THz imaging.

2D-ST THz imaging is used in a reflection configuration for the real-time monitoring of moving paint film and wet paint film.

A schematic of the experimental setup is shown in Fig. 10. A femtosecond Ti:sapphire regenerative amplifier (pulse energy = 1 mJ, pulse duration = 100 fs, central wavelength = 800 nm, repetition rate = 1 kHz) was employed to generate and detect intense THz pulses (not shown). An intense THz pulse was generated via the optical rectification of the pump light (pulse energy = 0.3 mJ) in a 4-mm-thick ⟨110⟩ ZnTe crystal (not shown). The THz beam was line-focused on the sample using a cylindrical THz lens (CL, f = 50 mm) with the focal line parallel to the y axis of the sample, resulting in a line of height (14 mm) being illuminated. Next, the line of the THz beam reflected from the sample was imaged by a THz lens (L1, f = 100 mm) onto a 1-mm-thick ⟨110⟩ ZnTe crystal for FSEOS. The width and imaging of THz focal line are influenced by the limited numerical aperture of CL and L1 compared with a transmission configuration (see Fig. 7). A 5 mm diameter probe beam (pulse energy = 1 μJ) was non-collinearly incident on the ZnTe with the THz beam at a crossed angle of θ in air. This resulted in the formation of a 2D-ST THz image on the ZnTe. FSEOS was then performed at the near-zero optical transmission point using two crossed polarizers (P and A).[28] Finally, the 2D-ST THz image was imaged onto a CCD camera in real-time via a lens (L2, f = 150 mm) as the 2D spatial distribution of the probe beam intensity. This 2D-ST THz image provided a Y–Z cross-sectional image of the sample.

Real-time THz reflection tomography of a moving paint film was demonstrated. The sample used in the experiment was a half-paint film in which the dry white alkyd painting was layered on half the area of an aluminum (Al) plate, as shown in Fig. 11(a). The paint thickness around the center of the painting area was 175 μm, which was measured beforehand using a contact, eddy-current-type thickness meter. The sample was continuously moved along the direction of the focus line (y axis in Fig. 10) using a translation stage (moving speed = 5 mm/s) when the THz beam was line-focused on the sample. A 2D-ST THz movie of the moving half-paint film corresponding to a 2D THz tomographic movie was measured at a frame rate of 10 frames/s when $\theta = 20°$.[29] Snapshots of the movie at three different illuminating positions (image size = 6 ps × 5 mm) that provided 2D cross-sectional images of the sample are shown in Fig. 11(b). In the unpainted area, one THz echo line from the surface of the Al plate appeared at approximately 2.8 ps. In the painted area, two THz echo lines from the paint surface (2.3 ps) and paint–substrate interface (4.5 ps) were clearly separated. The paint thickness was determined using the time delay and group refractive index of the paint (=2.14) because the time separation between the two echoes corresponded to the optical thickness of the paint film, as shown in the upper horizontal coordinate. The thickness resolution was determined to be 35 μm from the temporal duration of the THz pulse and a group refractive index of the sample. The 1D distribution of the paint thickness in the position range of 1–4 mm along the y axis of the sample in Fig. 11(b) was determined to be 162 ± 21 μm. This was based on the time separation between the two THz echoes, which was consistent with that measured by a contact-type thickness meter (= 175 μm). A mixture of one and two echoes was observed at the boundary between the unpainted and painted areas. It was considered that the blurring of the edge at the boundary between the two areas was mainly due to insufficient spatial resolution along the THz focal line (y axis) and/or the distorted temporal information caused by the scattering at the edge. Thus, the temporal evolution of 2D THz reflection tomography was clearly visualized as the illuminating position of the THz line beam moving across the sample.

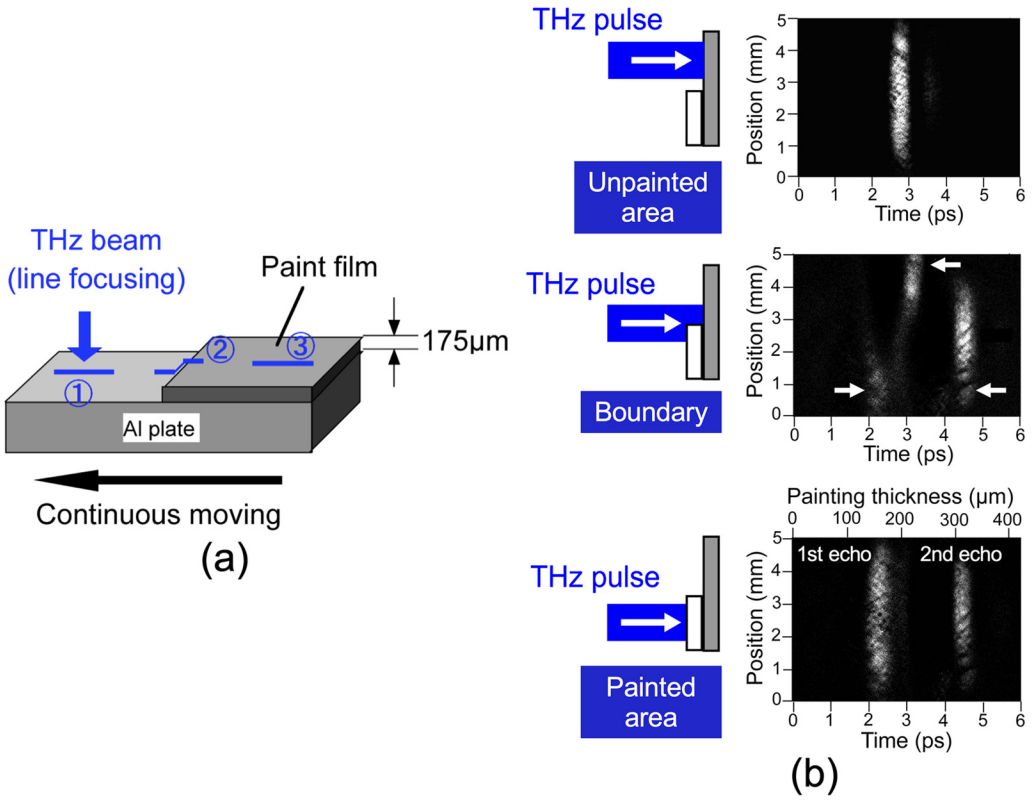

FIG. 11. (a) Sample of the moving paint film. (b) 2D cross-sectional images of the moving paint-film sample at three different illuminating positions (image size = 6 ps by 5 mm). The corresponding movie is given elsewhere.[29]

The remote sensing characteristics of THz reflection tomography enabled the monitoring of paint film thickness, even for wet paint. Conversely, conventional contact-type thickness meters cannot be applied in this situation. In this study, THz reflection tomography was applied to monitor the drying progress of a wet paint film via the temporal change of the paint film thickness through the wet-to-dry transformation. For this examination, a quick-drying white alkyd painting was made on an Al plate just before the start of the measurement. A THz tomographic movie of the drying process in the wet paint film was measured for 20 min immediately after the painting was completed.[30] Snapshots of the THz tomographic movie at 1 min intervals (image size = 6 ps × 5 mm) are shown in Fig. 12(a), demonstrating that two THz echo signals temporally evolved over the measurement period. The left echo line originated from the paint surface and, hence, was related to the geometric thickness of the paint film. The time separation between the left and right echo lines was related to the optical thickness of the paint film because the right echo line was a reflection from the paint–substrate interface. The temporal change of the first echo and the time separation with respect to the time passage are compared in Fig. 12(b). Error bar of each plot indicates the standard deviation of the first echo and time difference values along the THz focal line. Their temporal behaviors indicated that the geometrical and optical shrinkage of the paint film occurred during the wet-to-dry transformation. The temporal change was almost complete at 10 min because of the quick-drying paint, implying the completion of the drying process. Additionally, the shrinkage progressed uniformly in-plane, as shown in Fig. 12(a).[30] Furthermore, increasing the geometric thickness and decreasing the optical thickness do not match completely. This is because the former depends only on the geometric thickness variation, whereas the latter depends on both the geometric thickness variation and the group refractive index variation. The transfer or drying of the paint film would be completed before even a single cross-sectional image could be captured if the cross-sectional imaging of the wet paint film was performed using conventional point-to-point THz tomography. These demonstrations highlight the significant potential of 2D-ST THz imaging for reflection THz tomography.

IV. THZ SPECTRAL IMAGING OF MOVING OBJECTS

It is important to visualize both the geometrical shapes of internal structures and identify the chemical composition of test objects in the fields of nondestructive testing and evaluation. Spectroscopic analysis in the THz region has received interest as a new tool for material characterization because many materials

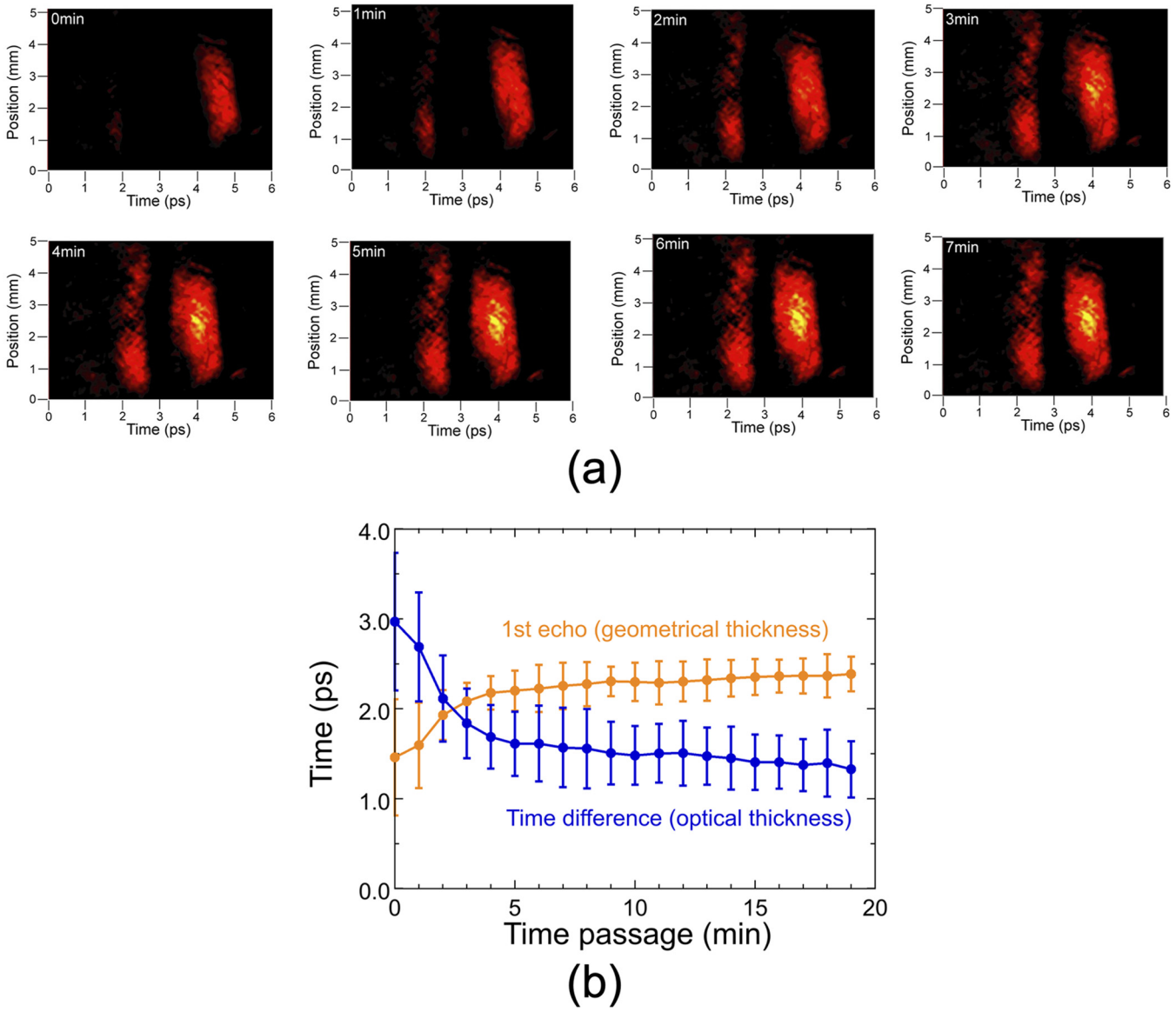

FIG. 12. (a) 2D cross-sectional images of the wet paint-film sample acquired at 1 min steps (image size = 6 ps by 5 mm). The corresponding movie is given elsewhere.[30] (b) Temporal change of the first echo and time separation with respect to time passage.

exhibit spectral fingerprints in the THz region.[1,5,24,31–33] THz spectral imaging provides a "color" perspective view of a sample in contrast to the conventional "gray" inspection achievable with x rays and ultrasound. The combined use of THz spectral images and fingerprints enables material characterization and spatial mapping. This approach shows promise for the screening of cancer tissues[7] and pharmaceutical tablets,[24] detecting explosives and illicit drugs,[31,32] and art conservation.[33] However, despite the advantages listed above, the THz spectral imaging technique is hampered by the slow speed of image acquisition, similar to THz reflection tomography. The real-time acquisition of a THz spectral line image can be achieved if 2D-ST THz imaging is combined with the Fourier transform of the time coordinate. In this section, 2D-ST THz imaging in a transmission configuration was combined with a Fourier transform for the THz spectral line imaging of moving objects.[18,19]

A schematic of the experimental setup is shown in Fig. 13. A pump light (pulse energy = 550 μJ, pulse duration = 100 fs, central wavelength = 800 nm, repetition rate = 1 kHz) radiated from a femtosecond Ti:sapphire regenerative amplifier passed through an

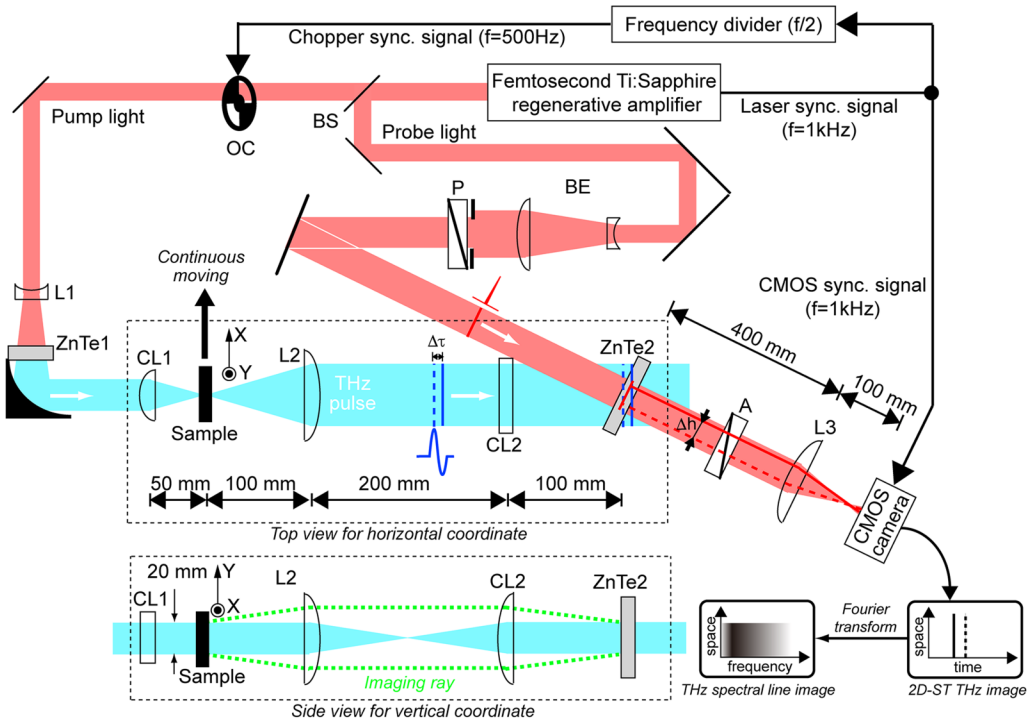

FIG. 13. Experimental setup of real-time THz spectral line imaging based on 2D-ST THz imaging.

optical chopper (OC) and a plano–concave lens (L1, f = −60 mm). A large-diameter, intense THz pulse was generated using the optical rectification of the pump light in a 1-mm-thick, 25-mm-square ⟨110⟩ ZnTe crystal (ZnTe1) and then fed into the optical system of THz beam and probe beam for 2D-ST THz imaging, which is given in Sec. II. C (see Fig. 7). The resulting 2D image of the probe beam was acquired using a high-speed CMOS camera (232 × 232 p, maximum frame rate = 1000 frame/s). To improve the SNR, we adopted a dynamic subtraction technique by synchronizing the camera to the 1 kHz laser pulses.[23] To this end, the pump beam is chopped using the OC to block every other laser pulse. We perform the alternate acquisition of probe images with and without the presence of the THz beam and then subtract successive images, thereby suppressing the background noise. The Fourier transformation of the horizontal axis in the 2D-ST THz image resulted in a THz spectral line image of the sample along the THz focal line or y axis. We here defined the spectral resolution as the increment of the discrete FFT spectra, which is limited by the pixel number of the horizontal axis in the camera. The sample was continuously moved across the THz focal line or along the x axis, to obtain a 2D spectral image of the sample using a mechanical stage while consecutively acquiring a series of line images. Subsequently, the individual line images were pieced together. The construction of a 2D spectral image using the successive stacking of real-time spectral line images is similar to the processing performed in general color scanners.

A four-segment metal hole array (4seg-MHA) made of stainless steel (SUS304) with a thickness of 300 μm was used as a sample to test the basic performance of this system.[18] Each of the four segments had different passbands (0.20, 0.40, 0.80, and 1.60 THz), as shown in Fig. 14(a). The MHA was continuously moved along the x axis at a rate of 1 mm/s using a translation stage because the THz beam was line-focused along the y axis onto the sample [see Fig. 14(b)]. Five hundred 2D-ST THz images per second were collected for 20 s (total number of acquired images = 10,000). Additionally, each group of 50 images was integrated to obtain 200 2D-ST THz images. The acquisition speed of the THz line image was 10 lines/s. Subsequently, THz spectral line images of the amplitude were obtained using Fourier transforming of the time dimension in the 2D-ST images. Finally, successive THz spectral images were obtained at an increment of frequency resolution of 29 GHz by rearranging a set of 200 recorded THz spectral line images regarding the THz frequency. We obtained 69 consecutive spectral images obtained at a frequency interval of 29 GHz within a frequency range of 2.01 THz. The THz spectral images selected at 0.20 0.41, 0.82, and 1.60 THz are shown in Fig. 14(c) (image size = 20 × 20 mm^2, corresponding to 200 × 232 p).[34] The crosstalk between the MHA segments was due to the bandpass characteristics of each MHA segment rather than the limited spectral resolution of the system. It is important to note that this movie is not a fast-forwarding movie but a "real-speed" movie of the measurement. Thus, the present system can

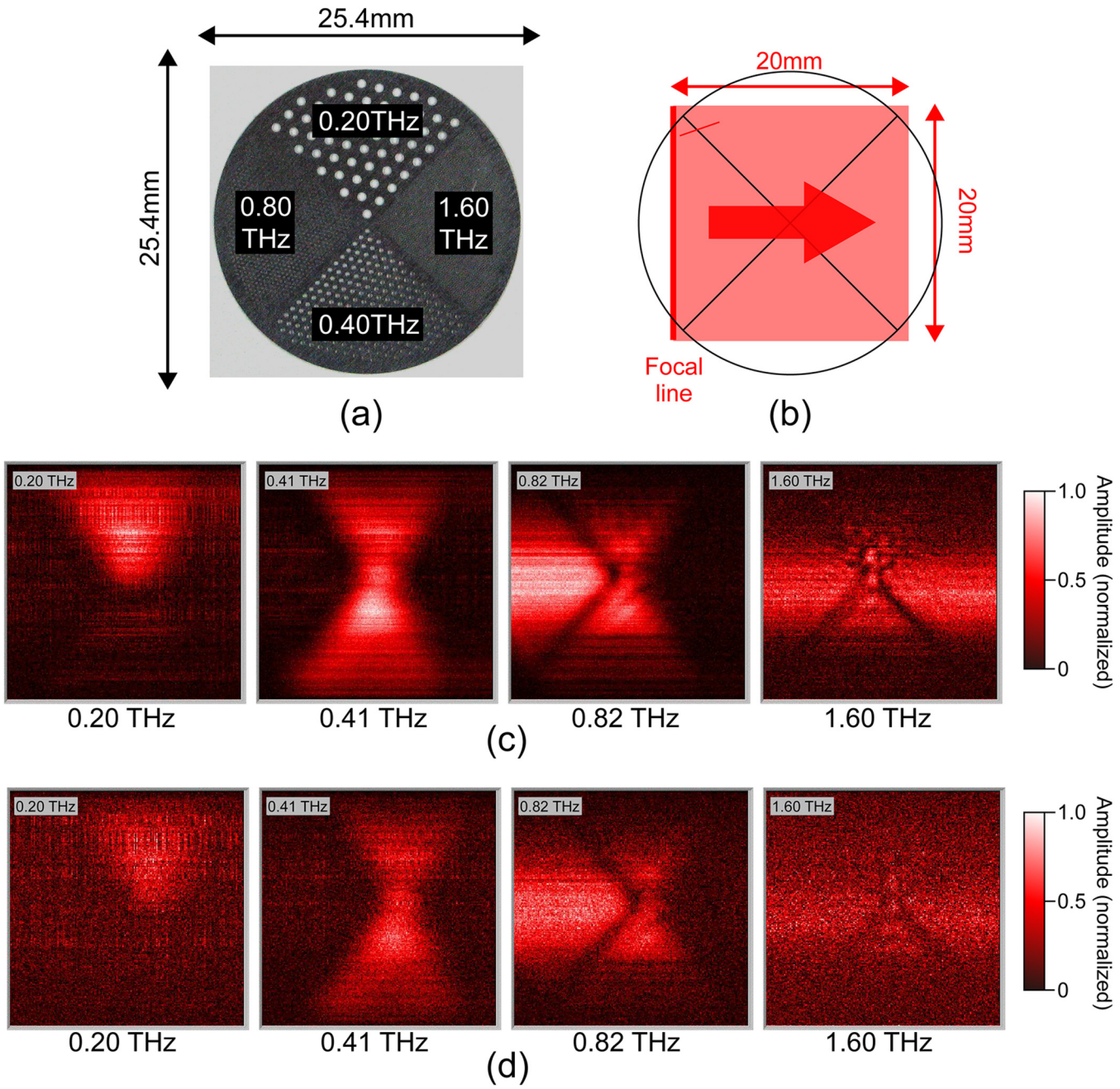

FIG. 14. THz spectral imaging of a moving four-segment metal hole array. (a) Photograph and (b) a schematic drawing of a four-segment metal hole array. (c) THz spectral images at moving speeds of 1 mm/s. The corresponding movie is given elsewhere.[34,35] (d) THz spectral images at moving speeds of 10 mm/s. The corresponding movie is given elsewhere.[36,37]

consecutively generate vertical line images of a moving sample in order, depending on the movement at all THz frequencies. The fade-out profile of the THz signal along the vertical direction was due to the Gaussian spatial distribution of the THz amplitude across the beam section, which was caused by the beam profile of the pump light. A flip video of all acquired THz spectral images for the 4seg-MHA (acquired time = 20 s) when the frequency was increased at an increment of spectral resolution (=29 GHz) was

demonstrated.[35] The frequency dependence of the spatial resolution and image SNR was confirmed, in addition to the spectral characteristics of the sample. The motion of the 4seg-MHA was increased to 10 mm/s to evaluate the limit on the speed of the sample. One thousand 2D-ST THz images were acquired for 2 s at 500 fps. Furthermore, groups of five images were integrated to maintain a sufficient number of vertical image lines (10 lines/mm) in the THz spectral images. THz spectral images and the corresponding movie of the 4seg-MHA at 0.20, 0.40, 0.82, and 1.60 THz are shown in Fig. 14(d) (image size = 20×20 mm^2, corresponding to 200×232 p).[36] Even at a sample speed of 10 mm/s, the THz spectral images at 0.20, 0.4, and 0.82 THz exhibited the spectral characteristics of the 4seg-MHA, despite the decreased SNR. The signal for the 1.60 THz MHA segment was quite low in the THz spectral image at 1.60 THz, which was mainly due to the decreased SNR and limited dynamic range of the signal at higher THz frequencies. A flip video of all acquired THz spectral images (acquired time = 2 s) for the 4seg-MHA when the frequency was increased at an increment of the spectral resolution (= 29 GHz) was demonstrated.[37] In this case, the pixel rate was 23,200 p/s based on the total number of image pixels (= 46,400 p) and image acquisition time (= 2 s). This is several orders of magnitude higher than conventional point-to-point THz time-domain spectroscopy (THz-TDS) imaging.

Quality control of pharmaceutical tablets is a promising application of THz spectral imaging because many medicines demonstrate sharp spectral fingerprints in the THz region that result from their crystal structures.[1,24] However, the scope of this application does not include *in-line* total inspection during the manufacturing process because of the slow imaging rate. Instead, the potential of the proposed system is demonstrated for the rapid nondestructive classification of pharmaceutical tablets moving on a translation stage. Three sugar tablets (D-glucose, D-maltose, and lactose powders mixed with polyethylene powder) and one reference tablet (polyethylene powder) of identical shapes (diameter = 10 mm and thickness = 1 mm) were prepared. The three sugar tablets exhibited the characteristic spectral fingerprints of THz absorption: 1.44 THz for D-glucose, 1.10 and 1.61 THz for D-maltose, and 0.53 and 1.37 THz for lactose.[19] These were set in a sample holder made of a polyethylene plate and concealed in a paper envelope to simulate an application for packaged objects. One hundred and sixteen consecutive spectral images of the THz transmittance of the sample were acquired at a frequency interval of 26 GHz within a frequency range of 0–2.98 THz. The THz power transmittance images of the samples (image area = 60×20 mm^2, size = 600×232 p, image acquisition time = 60 s) extracted at four different frequencies appearing in the THz spectral fingerprints are shown in Fig. 15.[38] The blue color in these images corresponds to low transmittance and, therefore, high absorption. Low-transmittance images appeared at 0.51 and 1.41 THz for the first tablet, 1.07 and 1.61 THz for the second tablet, and 1.41 THz for the fourth tablet. The third tablet did not exhibit low-transmittance images at any frequency. From these results, we determined that the first, second, third, and fourth samples were the lactose, D-maltose, reference, and D-glucose tablets, respectively. The horizontal stripe-type noise observed on the image was mainly due to the uneven detection sensitivity of ZnTe2 and/or scattering of the probe light, caused by residual birefringence, defects, and impurities in ZnTe2.

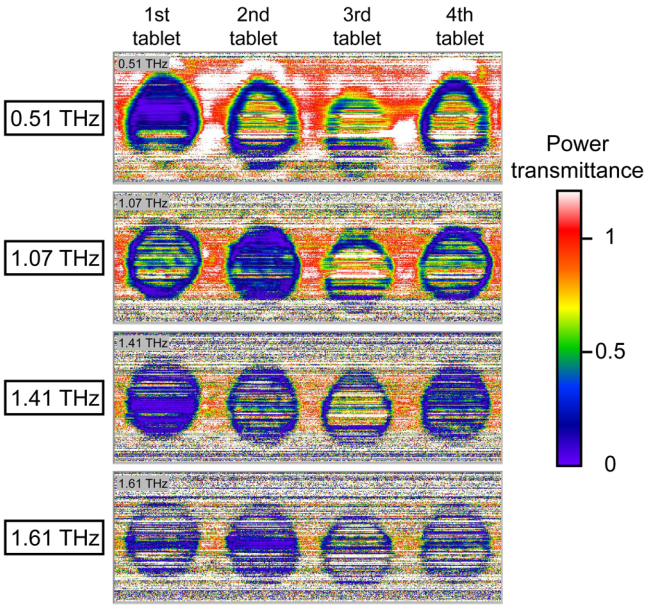

FIG. 15. THz spectral imaging of moving pharmaceutical tablets. The corresponding movie is given elsewhere.[38]

A human tooth sample (sliced molar, thickness = 0.5 mm) was also measured to investigate the potential of THz spectral imaging for biological imaging of hard tissues. Seventy-nine consecutive spectral images of the THz transmittance of the sample were acquired at a frequency interval of 26 GHz within a frequency range of 0–2.02 THz. Extracted spectral images of the THz power transmittance at fourteen different frequencies (image size = 20 mm in height × 20 mm in width, number of pixels = 232×240, image acquisition time = 240 s, image acquisition rate = 1 line/s, pixel rate = 232 p/s) are shown in Fig. 16 (Multimedia view), in which consecutive spectral images of THz power transmittance are shown. The characteristic distribution of the THz power transmittance was observed depending on the sample position. Furthermore, the spatial distribution of the transmittance changed with respect to the THz frequency. The outer portion of the specimen absorbed the THz waves more strongly than the inner portion at lower THz frequencies. Conversely, there were no large differences in the THz transmittance between the inner and outer portions at higher THz frequencies. Differences in the crystal structure between different tissues and/or the portion-dependence of the crystal structure may be reflected in the characteristic spectral fingerprints in the THz region because THz spectral fingerprints are common to many crystalline materials.[1,24,31,32]

V. RAPID THZ CT FOR 2D SPECTRAL CROSS-SECTIONAL AND 3D VOLUMETRIC IMAGING

CT is a ubiquitous technique that provides 2D cross-sectional or 3D volumetric images of objects in transmission configuration. The reconstruction of these images was performed by analyzing a

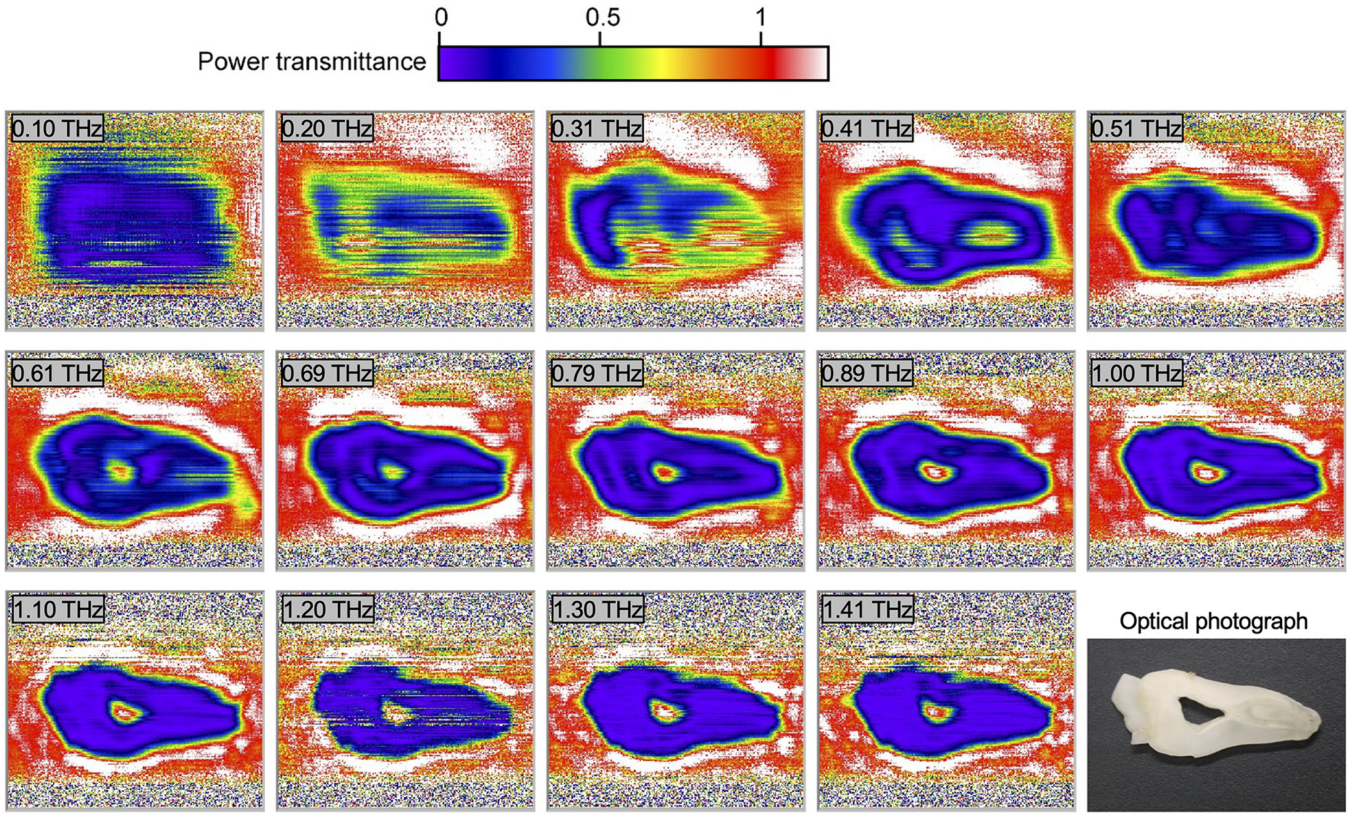

FIG. 16. THz spectral imaging of moving sliced tooth sample. Multimedia available online.

series of projection images at different projection angles using the filtered back-projection (FBP) algorithm.[39] Although this imaging modality has been widely used in combination with x rays, its high penetration and invasiveness often limit what can be measured. However, THz pulses can provide complementary CT methods owing to their low photon energy and moderate penetration in dry, non-polar, and soft materials, such as plastics,[8] wood,[40] bone,[8] and pharmaceutical tablet.[41] Furthermore, the THz pulse effectively provided the spectral CT of the test object in the THz range for material characterization. However, THz CT based on a point-to-point THz-TDS system requires an additional mechanical scan of sample rotation to acquire a series of projection images, in addition to multiple mechanical scans of time delay and sample position. This leads to a lengthy image acquisition time. 2D-ST THz imaging was applied to THz CT to significantly reduce the image acquisition time.

To obtain a 2D spectral cross-sectional image of a sample using THz CT, a series of projection line images with temporal information of the THz pulse must be acquired using three types of mechanical scans: time delay, 1D sample position, and sample rotation. Only a mechanical scan of a sample rotation is required if 2D-ST THz imaging is applied to real-time spectral line projection in THz CT. The experimental setup of rapid THz CT is shown in Fig. 17, in which two parts of the real-time THz spectral line imaging system were modified (see Fig. 13). The first modification was in the optical system for generating an intense THz pulse. Cherenkov radiation from a $LiNbO_3$ crystal excited by a pulse-front-tilted pump beam[42,43] was used to increase the THz pulse energy by a factor of 10 and, hence, decrease the image acquisition time by a factor of 100.[21] The pump beam was incident onto an Au-coated 2000 mm/line holographic grating to introduce the desired pulse front tilt and satisfy the phase-matching condition for optical rectification in a stoichiometric $LiNbO_3$ crystal (1.5% Mg concentration). The appropriate tilt angle of the pump pulse wavefront in the crystal was controlled by a combination of the grating and two lenses (L1, $f = 200$ mm; L2, $f = 100$ mm). Finally, the pump beam was focused onto the crystal with a spot size of 2×2 mm^2. One surface of the crystal was cut with a phase-matching angle of 62°. The resulting intense THz pulse was used for the THz optical system (green beam in Fig. 17). The second modification was the line focusing of the THz beam across the cross section of the sample (y axis in Fig. 17) using a THz cylindrical lens (THz-CL1, $f = 100$ mm). That is, the THz focal line is along the axial direction of the sample in Fig. 13, whereas it is across the sample in Fig. 17. These modifications enabled a real-time line projection of the THz beam on the sample

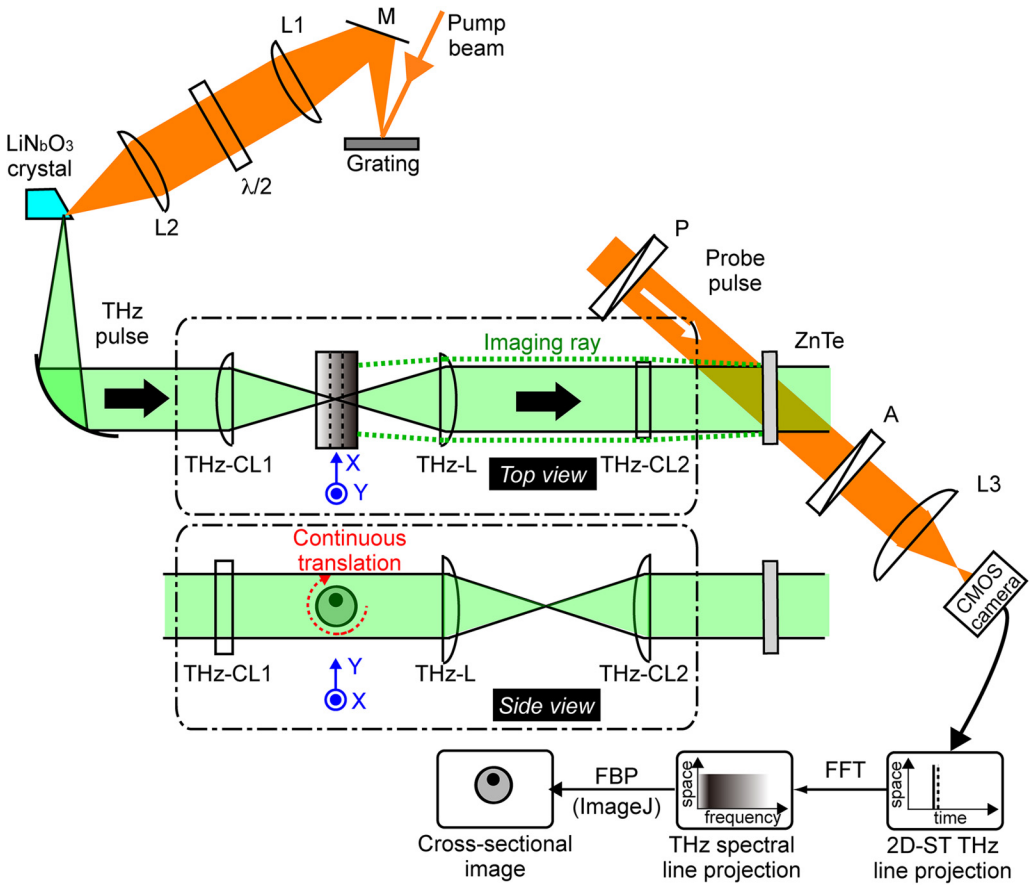

FIG. 17. Experimental setup of rapid THz CT for real-time spectral line projection based on 2D-ST THz imaging.

to be achieved. The THz beam passing through the sample was then used for 2D-ST THz imaging after passing through a THz plano–convex lens (THz-L, f = 100 mm) and a THz cylindrical lens (THz-CL2, f = 100 mm). The resulting 2D-ST THz image had a temporal range of 37 ps and spatial range of 15 mm. The Fourier transformation of the time axis in the 2D-ST THz image provided spectral line projection data for the sample (spectral resolution = 27 GHz). The sample was rotated through a full turn using continuous rotation for 6 s. During this rotation, 600 line-projection datasets of a 2D-ST THz image were collected at a rate of 100 Hz, resulting in an angular sampling resolution of only 0.6°. In traditional THz-CT, only 18 (angular step of 10°) or 36 (angular step of 5°) projection angles can be selected owing to the long acquisition time of the point-by-point and angle-by-angle scanning measurements (more than 1h). Therefore, a significant advantage of the proposed system over the conventional systems is its ability to perform fast and precise CT imaging. Finally, the spectral cross section of the sample across the THz focal line was reconstructed by analyzing a spectral line projection data series, that is, a sinogram, using the FBP algorithm implemented in the ImageJ software.[39,44]

A simple sample was investigated to demonstrate rapid cross-sectional reconstruction that consisted of four metallic bars (2 mm diameter) without THz spectral fingerprints, illuminated by a THz focal line, as shown in Fig. 18(a). A sinogram of the spectral amplitude at 0.60 THz for this sample is shown in Fig. 18(b), where the horizontal and vertical coordinates provided the rotation angle (600 points from 0 to 360°) and THz projection-line image (232 points from 0 to 15 mm). The white color indicates a decrease in the spectral amplitude. An isolated distribution of the four metallic bars generated four overlapping sinusoidal waveforms in the sinogram for different phases of the rotation angle. A cross-sectional image corresponding to a portion of the object illuminated by the THz line was reconstructed, as shown in Fig. 18(c). White and black indicate the weak and strong signals in the THz spectral amplitude, respectively. Therefore, the white regions in Fig. 18(c) visualize structures where the signal decreased. Although no spectroscopic information could be obtained from this metallic sample, the positions and shapes of the four metallic bars were clearly visualized, demonstrating the ability of the system to properly reconstruct the cross-sectional images of simple samples in only 6 s.

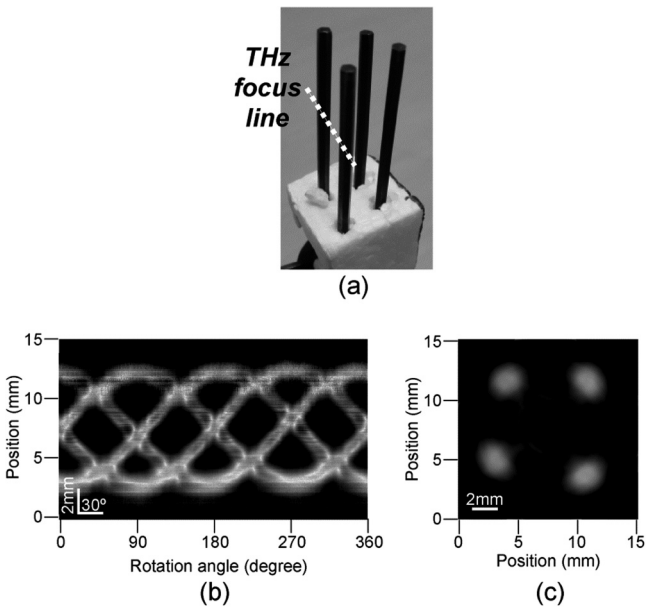

FIG. 18. 2D spectral cross-sectional imaging of four metallic bars. (a) Optical photograph. (b) Sinogram of the spectral amplitude at 0.6 THz. (c) 2D cross-sectional image at 0.6 THz.

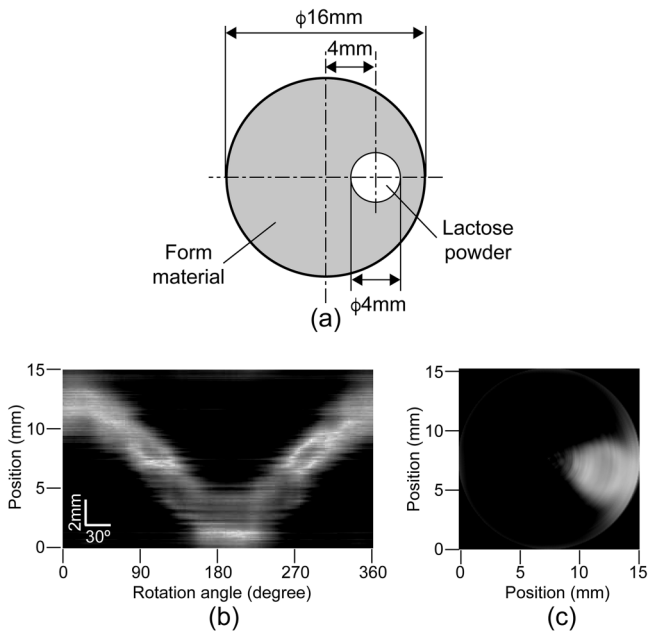

FIG. 19. 2D spectral cross-sectional imaging of lactose powder contained in a cylindrical hole of the foam cylinder. (a) Schematic drawing of the sample. (b) Sinogram of the spectral amplitude at 0.53 THz. (c) 2D cross-sectional image at 0.53 THz.

The second sample was a foam cylinder (16 mm diameter), in which an off-axis cylindrical hole (4 mm diameter) was drilled, as shown in Fig. 19(a). To demonstrate the THz spectral CT, the hole was filled with lactose powder mixed with polyethylene powder (30-w% lactose and 70-w% polyethylene; spectral fingerprint = 0.51 THz). A sinogram of the spectral amplitude at 0.53 THz and the corresponding reconstructed spectral cross section of the sample are shown in Figs. 19(b) and 19(c), respectively. The area of the foam cylinder was not visible owing to the low refractive index change from air to foam and the low absorption coefficient of the foam. The position and size of the cylindrical hole were revealed owing to the different transmission of THz radiation in this part of the sample, as shown in Figs. 19(b) and 19(c). The lower transmission was due to refraction loss and lactose absorption at 0.53 THz.

To further extend 2D THz CT into 3D volumetric imaging or 3D THz CT, a series of projection 2D images with temporal information of the THz pulse must be acquired using four types of mechanical scans: time delay, 2D sample position (horizontal and vertical positions), and sample rotation. However, only the sample vertical position and sample rotation mechanical scans are required here if 2D-ST THz imaging is applied for 3D THz CT. The experimental setup of the THz CT for 3D volumetric imaging, namely, 3D THz CT, is shown in Fig. 20. The differences between the experimental setups of 2D THz CT (Fig. 17) and 3D THz CT (Fig. 20) are the method of irradiating the sample with the THz beam and the required mechanical scanning mechanism. The THz beam was line-focused onto the sample using a THz cylindrical lens (THz-CL1, f = 50 mm), resulting in a line of illumination along the y axis (length = 25 mm, width = 1 mm) across the sample. Next, the THz line was imaged along the vertical y axis of a (110)-oriented ZnTe crystal (thickness = 1 mm, size = 25 × 25 mm^2) using the combination of a THz plano–convex lens (THz-L, f = 50 mm) and THz cylindrical lens (THz-CL2, f = 50 mm). For 2D-ST THz imaging, the probe beam was non-collinearly incident on the ZnTe crystal at a crossed angle of 25° with the THz beam. The spatial intensity distribution of the probe beam was obtained after passing through two crossed polarizers (P and A). The pixel value was extracted for each projection angle at every horizontal and vertical sample position by measuring the peak-to-peak value of the THz electric field in the temporal waveform. We here used the peak-to-peak value because of a relatively high SNR compared with the THz spectral peak of amplitude. Subsequently, the application of the well-known FBP algorithm implemented in the ImageJ software numerically provided the multiplanar slices of the sample to reconstruct the 3D volume.[39,44]

The first test sample was a plastic box (10 × 10 mm^2) with a wooden toothpick inside that was illuminated by the vertical THz focal line, as shown in the inset in Fig. 21(a). 3D CT was performed in only 6 min after continuous horizontal translation (2 mm/s, 100 p) of the sample and 36 rotations with a 5° angle increment to collect the projection data. The 3D reconstruction of the sample was obtained using ImageJ software,[44] as shown in Fig. 21(a) and its corresponding movie,[45] in which white and black indicate the weak and strong transmitted THz signals, respectively. First, the position of the toothpick inside the plastic box was able to be

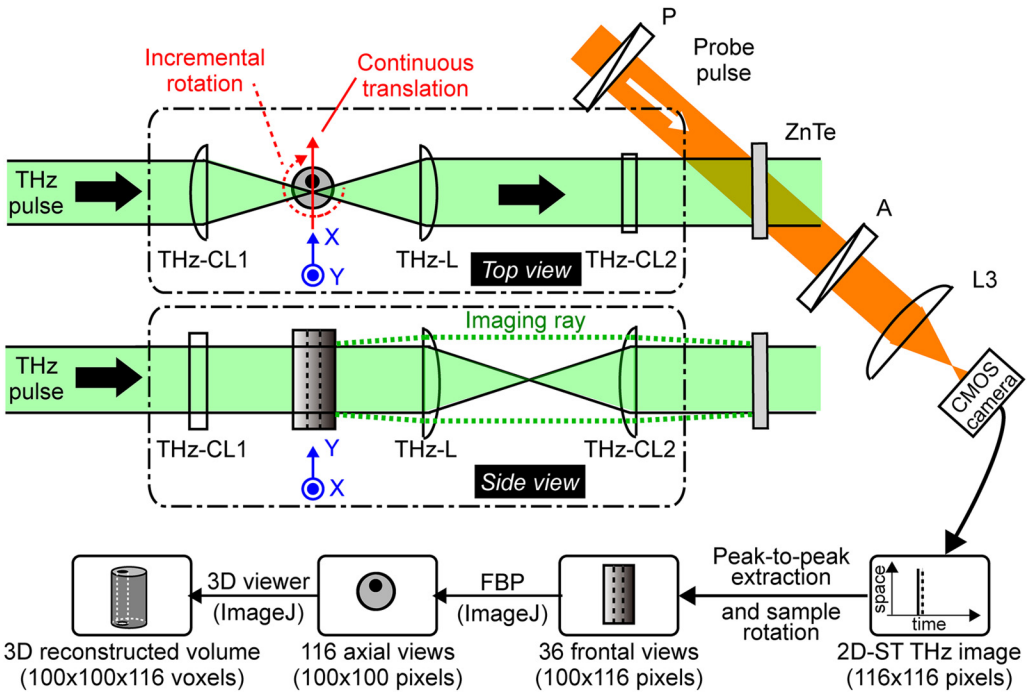

FIG. 20. Experimental setup of rapid THz CT for 3D volumetric imaging based on 2D-ST THz imaging.

determined. Second, the shape of the rectangular plastic box was not perfectly reconstructed. This was because the relative transparency of the plastic material for THz radiation produced a weak attenuation of the transmitted THz pulse, except around the four corners, which were more clearly visible in the figure. This example demonstrates the ability of the system to properly reconstruct the 3D shapes of simple samples in a relatively short time.

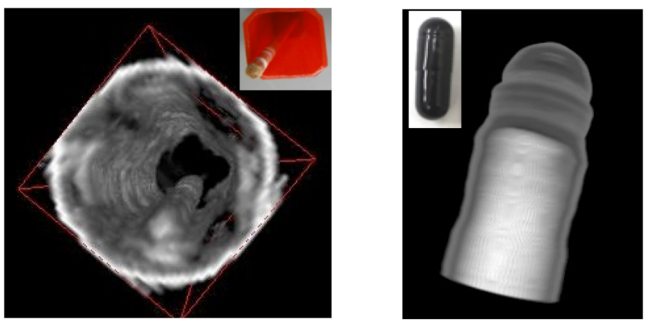

FIG. 21. 3D volumetric images. (a) Plastic box ($10 \times 10\ mm^2$) with a wooden toothpick inside. The corresponding movie is given elsewhere.[45] (b) Gelatin-soluble capsule enclosing a dose of medicine powder. The corresponding movie is given elsewhere.[46]

The 3D volumetric images of a gelatin-soluble capsule enclosing a dose of medicine powder [inset in Fig. 21(b), object size: $7 \times 20\ mm^2$] were also visualized. This represents a more realistic object to test the potential of the system for pharmaceutical applications. The 3D reconstruction of the capsule is shown in Fig. 21(b) and its corresponding movie.[46] It is possible to clearly see the capsule with the localization of its internal content. Here, the THz radiation was completely absorbed by the medicine powder. It was clearly not possible to obtain any information about the chemical component of the medicine powder from the peak-to-peak analysis of the THz electric field. This would require a spectroscopic analysis of the 2D-ST image. Additionally, the spectral amplitude at a given frequency can be extracted for 3D spectral volume imaging after the fast Fourier transform of the temporal data.

VI. SUMMARY AND OUTLOOK

Real-time imaging of moving objects is the key to developing various real-world applications using THz imaging. Unfortunately, the most popular THz-TDS systems are based on time-consuming point scanning that can only be used for spot inspection and not for the total inspection of moving objects. 2D-FSEOS enables the 2D real-time THz imaging of a moving object at a fixed time delay. However, THz imaging at a fixed time delay merely provides a gray-scale image of shadowgraph without any temporal or spectral information, in the same manner as an x ray. Such gray-scale THz shadowgraphs undermine the high functionality of coherent THz imaging, which spoils the temporal or spectral information of

THz pulses. This Tutorial focused on 2D-ST THz imaging based on the combination of non-collinear 2D-FSEOS and real-time THz line imaging to provide coherent THz high-speed imaging characteristics applicable to the total inspection of moving objects without compromising its high functionality. While a gray-scale THz shadowgraph at a fixed time delay based on 2D-FSEOS uses 2D coordinates that can be acquired by a camera in the 2D spatial information of a sample, 2D-ST THz imaging uses the 2D camera coordinates in the 1D spatial and 1D temporal information of a sample. This change produces a large difference in the imaging rate because mechanical time-delay scanning is the most significant factor in slowing the imaging speed. Furthermore, in the total inspection of the manufacturing process, the 2D spatial information of objects is not necessarily required because the objects are continuously moving in one direction on a translation stage. A 2D image of a sample is automatically generated according to the movement of an object, as long as the 1D spatial information corresponding to the line image is acquired in real-time. In this way, it is sufficient to obtain only 1D spatial information, so the remaining 1D coordinate in a camera can be used for the temporal information of a sample in 2D-ST THz imaging. It should be emphasized that the incomparable high-speed data acquisition achieved by 2D-ST THz imaging facilitates THz tomographic and spectral imaging of moving objects.

First, 2D-ST THz imaging was applied to the real-time THz reflection tomography of paint films in a reflection configuration. The temporal evolution of the 2D cross-sectional images was clearly visualized as the illuminating position of the THz beam moved across the paint sample. Real-time monitoring of the thickness and drying dynamics were also demonstrated in a wet paint film. Second, 2D-ST THz imaging was applied to the THz spectral imaging of moving objects in a transmission configuration. The Fourier transform of the time axis in the 2D-ST THz image enabled the THz spectral line image of the sample. Additionally, the ability to distinguish and spatially image three different sugar tablets was demonstrated by employing the real-time line scanning of a THz beam. This demonstration indicated the potential of the THz color scanner in total inspection for the rapid quality control of objects moving on a translation stage. Third, 2D-ST THz imaging was applied to rapid THz CT. The potential of real-time THz line projection was demonstrated for the 2D spectral cross-sectional imaging of continuously rotating objects. Line projection data were recorded in real-time in association with the continuous rotation of the sample owing to the 10 ms acquisition time of the 2D-ST THz image. Finally, the potential of THz CT for 3D volumetric imaging was proven. To the best of our knowledge, this is the first time that coherent THz imaging techniques have been applied to moving objects, owing to their real-time capability. These rapid, functional, coherent THz imaging techniques based on 2D-ST THz imaging will be powerful tools for sensing, nondestructive inspection, and material characterization of moving objects in practical applications.

A remaining challenge for THz generation in 2D-ST THz imaging is the use of an expensive, bulky femtosecond Ti:sapphire regenerative amplifier. A less expensive, less cumbersome laser source alternative is a femtosecond ytterbium-doped fiber laser, which has sufficient pulse energy to generate an intense THz pulse via the optical nonlinear effect.[47] Although Cherenkov radiation from a $LiNbO_3$ crystal excited by a pulse-front-tilted pump beam is a promising approach to generate intense THz pulses, its experimental setup is relatively complicated and precise adjustment of the pulse-front-tilted pump beam to the crystal is required. The use of a grating-engraved $LiNbO_3$ crystal may be one means of solving this problem.[48–51] A remaining challenge for THz detection is to extend the size of the time and space axes in a 2D-ST THz image, which is limited by the size of the ZnTe crystal for non-collinear 2D-FSEOS. In addition to the increase in the size to 100 mm^2 or more, it is important to improve the quality of the crystal by reducing internal defects and homogenizing residual birefringence. If all of these problems are solved, the social implementation of 2D-ST imaging will be further accelerated.

ACKNOWLEDGMENTS

The authors thank Dr. Mukesh Jewariya for his experimental support. The authors also acknowledge the financial support for the project from the Promotion of Regional Industries and Universities by the Cabinet Office, Government of Japan, as well as from the Plan for Industry Promotion and Young People's Job Creation by the Creation and Application of Next-Generation Photonics by Tokushima Prefecture, Japan.

AUTHOR DECLARATIONS

Conflict of Interest

The authors have no conflicts to disclose.

Author Contributions

Takeshi Yasui: Conceptualization (equal); Data curation (equal); Formal analysis (equal); Funding acquisition (lead); Investigation (equal); Methodology (equal); Project administration (equal); Resources (equal); Software (supporting); Supervision (equal); Validation (equal); Visualization (lead); Writing – original draft (lead); Writing – review & editing (supporting). **Emmanuel Abraham:** Conceptualization (equal); Data curation (equal); Formal analysis (equal); Funding acquisition (supporting); Investigation (equal); Methodology (equal); Project administration (equal); Resources (equal); Software (lead); Supervision (equal); Validation (equal); Visualization (lead); Writing – original draft (supporting); Writing – review & editing (lead).

DATA AVAILABILITY

The data that support the findings of this study are available from the corresponding author upon reasonable request.

REFERENCES

[1]M. Tonouchi, Nat. Photonics **1**, 97–105 (2007).
[2]C. Jansen, S. Wietzke, O. Peters, M. Scheller, N. Vieweg, M. Salhi, N. Krumbholz, C. Jördens, T. Hochrein, and M. Koch, Appl. Opt. **49**, E48 (2010).
[3]H. Guerboukha, K. Nallappan, and M. Skorobogatiy, Adv. Opt. Photonics **10**, 843 (2018).
[4]D. M. Mittleman, Opt. Express **26**, 9417 (2018).
[5]B. B. Hu and M. C. Nuss, Opt. Lett. **20**, 1716 (1995).

[6]D. M. Mittleman, S. Hunsche, L. Boivin, and M. C. Nuss, Opt. Lett. **22**, 904 (1997).
[7]T. Löffler, T. Bauer, K. Siebert, H. Roskos, A. Fitzgerald, and S. Czasch, Opt. Express **9**, 616 (2001).
[8]B. Ferguson, S. Wang, D. Gray, D. Abbot, and X.-C. Zhang, Opt. Lett. **27**, 1312 (2002).
[9]H.-T. Chen, R. Kersting, and G. C. Cho, Appl. Phys. Lett. **83**, 3009 (2003).
[10]T. Yasui, E. Saneyoshi, and T. Araki, Appl. Phys. Lett. **87**, 061101 (2005).
[11]C. Janke, M. Först, M. Nagel, H. Kurz, and A. Bartels, Opt. Lett. **30**, 1405 (2005).
[12]S. Kray, F. Spöler, T. Hellerer, and H. Kurz, Opt. Express **18**, 9976 (2010).
[13]Y. Kim and D.-S. Yee, Opt. Lett. **35**, 3715 (2010).
[14]Q. Wu, T. D. Hewitt, and X.-C. Zhang, Appl. Phys. Lett. **69**, 1026 (1996).
[15]R. I. Stantchev, X. Yu, T. Blu, and E. Pickwell-MacPherson, Nat. Commun. **11**, 2535 (2020).
[16]J. Shan, A. S. Weling, E. Knoesel, L. Bartels, M. Bonn, A. Nahata, G. A. Reider, and T. F. Heinz, Opt. Lett. **25**, 426 (2000).
[17]T. Yasuda, T. Yasui, T. Araki, and E. Abraham, Opt. Commun. **267**, 128 (2006).
[18]T. Yasui, K. Sawanaka, A. Ihara, E. Abraham, M. Hashimoto, and T. Araki, Opt. Express **16**, 1208 (2008).
[19]M. Schirmer, M. Fujio, M. Minami, J. Miura, T. Araki, and T. Yasui, Biomed. Opt. Express **1**, 354 (2010).
[20]E. Abraham, Y. Ohgi, M. Minami, M. Jewariya, M. Nagai, T. Araki, and T. Yasui, Opt. Lett. **36**, 2119 (2011).
[21]M. Jewariya, E. Abraham, T. Kitaguchi, Y. Ohgi, M. Minami, T. Araki, and T. Yasui, Opt. Express **21**, 2423 (2013).
[22]Q. Wu and X. C. Zhang, Appl. Phys. Lett. **67**, 3523 (1995).
[23]F. Miyamaru, T. Yonera, M. Tani, and M. Hangyo, Jpn. J. Appl. Phys. **43**, L489 (2004).
[24]Y.-C. Shen and P. F. Taday, IEEE J. Sel. Top. Quantum Electron. **14**, 407 (2008).
[25]T. Yasui, T. Yasuda, K. Sawanaka, and T. Araki, Appl. Opt. **44**, 6849 (2005).
[26]T. Yasuda, T. Iwata, T. Araki, and T. Yasui, Appl. Opt. **46**, 7518 (2007).
[27]R. M. Woodward, B. E. Cole, V. P. Wallace, R. J. Pye, D. D. Arnone, E. H. Linfield, and M. Pepper, Phys. Med. Biol. **47**, 3853 (2002).
[28]Z. Jiang, F. G. Sun, Q. Chen, and X.-C. Zhang, Appl. Phys. Lett. **74**, 1191 (1999).
[29]See https://ars.els-cdn.com/content/image/1-s2.0-S0030401806005761-mmc1.gif for information about 2D cross-sectional movie of the moving paint-film sample.
[30]See https://ars.els-cdn.com/content/image/1-s2.0-S0030401806005761-mmc2.gif for information about 2D cross-sectional movie of drying process in the wet paint-film.
[31]Y. C. Shen, T. Lo, P. F. Taday, B. E. Cole, W. R. Tribe, and M. C. Kemp, Appl. Phys. Lett. **86**, 241116 (2005).
[32]K. Kawase, Y. Ogawa, Y. Watanabe, and H. Inoue, Opt. Express **11**, 2549 (2003).
[33]J. B. Jackson, J. Bowen, G. Walker, J. Labaune, G. Mourou, M. Menu, and K. Fukunaga, IEEE Trans. Terahertz Sci. Tech. **1**, 220 (2011).
[34]See http://opg.optica.org/viewmedia.cfm?uri=oe-16-2-1208-2 for information about THz spectral movie of 4seg-MHA at moving speeds of 1 mm/s.
[35]See http://opg.optica.org/viewmedia.cfm?uri=oe-16-2-1208-5 for information about flip video of all acquired THz spectral images for 4seg-MHA at moving speeds of 1 mm/s.
[36]See http://opg.optica.org/viewmedia.cfm?uri=oe-16-2-1208-3 for information about THz spectral movie of 4seg-MHA at moving speeds of 10 mm/s.
[37]See http://opg.optica.org/viewmedia.cfm?uri=oe-16-2-1208-6 for information about flip video of all acquired THz spectral images for 4seg-MHA at moving speeds of 10 mm/s.
[38]See http://opg.optica.org/viewmedia.cfm?uri=boe-1-2-354-1 for information about flip video of all acquired THz spectral images for moving pharmaceutical tablets.
[39]G. T. Herman, *Fundamentals of Computerized Tomography: Image Reconstruction From Projections* (Springer Science & Business Media, Berlin, 2009).
[40]B. Recur, A. Younus, S. Salort, P. Mounaix, B. Chassagne, P. Desbarats, J.-P. Caumes, and E. Abraham, Opt. Express **19**, 5105 (2011).
[41]A. Brahm, M. Kunz, S. Riehemann, G. Notni, and A. Tünnermann, Appl. Phys. B **100**, 151 (2010).
[42]J. Hebling, K.-L. Yeh, M. C. Hoffmann, B. Bartal, and K. A. Nelson, J. Opt. Soc. Am. B **25**, B6–B19 (2008).
[43]M. Jewariya, M. Nagai, and K. Tanaka, J. Opt. Soc. Am. B **26**, A101 (2009).
[44]W. S. Rasband, See http://imagej.nih.gov/ij/ for ImageJ (U.S. National Institutes of Health, Bethesda, MD) 1997–2012.
[45]See http://opg.optica.org/viewmedia.cfm?uri=oe-21-2-2423-3 for information about 3D volumetric movie of plastic box with a wooden toothpick inside.
[46]See http://opg.optica.org/viewmedia.cfm?uri=oe-21-2-2423-5 for information about 3D volumetric movie of gelatin-soluble capsule enclosing a dose of medicine powder.
[47]M. Nagai, E. Matsubara, M. Ashida, J. Takayanagi, and H. Ohtake, IEEE Trans. Terahertz Sci. Technol. **4**, 440–446 (2014).
[48]L. Pálfalvi, J. A. Fülöp, G. Almási, and J. Hebling, Appl. Phys. Lett. **92**, 171107 (2008).
[49]K. Nagashima and A. Kosuge, Jpn. J. Appl. Phys. **49**, 122504 (2010).
[50]K. Nagashima, M. Tsubouchi, Y. Ochi, and M. Maruyama, J. Appl. Phys. **123**, 123104 (2018).
[51]P. S. Nugraha, G. Krizsán, C. Lombosi, L. Pálfalvi, G. Tóth, G. Almási, J. A. Fülöp, and J. Hebling, Opt. Lett. **44**, 1023 (2019).